A case study on spin-state effect of iron catalysis

Peng He[1], Meng-Yang Hu[1], Jin-Hong Li[1], Tian-Zhang Qiao[1], Yi-Lin Lu[1], Shou-Fei Zhu*[,1,2]

[1] *Frontiers Science Center for New Organic Matter, State Key Laboratory and Institute of Elemento-Organic Chemistry, Nankai University, Tianjin 300071, China*

[2] *Haihe Laboratory of Sustainable Chemical Transformations, Tianjin 300192, China*

** Email: sfzhu@nankai.edu.cn*

Abstract: Iron catalysts are ideal transition metal catalysts because of the Earth abundant, cheap, biocompatible features of the iron salts. Iron catalysts often have unique open-shell structures that easily undergo spin crossover in chemical transformations, a feature rarely found in noble metal catalysts. Unfortunately, little is known currently about how the open-shell structure and spin crossover affect the reactivity and selectivity of iron catalysts, which makes the development of iron catalysts a low efficient trial-and-error program. In this paper, a combination of experiments and theoretical calculations revealed that the iron-catalyzed hydrosilylation of alkynes is typical spin-crossover catalysis. Deep insight into the electronic structures of a set of well-defined open-shell active formal Fe(0) catalysts revealed that the spin-delocalization between the iron center and the 1,10-phenanthroline ligand effectively regulates the iron center's spin and oxidation state to meet the opposite electrostatic requirements of oxidative addition and reductive elimination, respectively, and the spin crossover is essential for this electron transfer process. The triplet transition state was essential for achieving high regioselectivity

through tuning the nonbonding interactions. These findings provide an important reference for understanding the effect of catalyst spin state on reaction. It is inspiring for the development of iron catalysts and other Earth-abundant metal catalysts, especially from the point of view of ligand development.

Keywords: spin-state effect • spin-delocalization • spin crossover • iron-catalysis • alkyne hydrosilylation

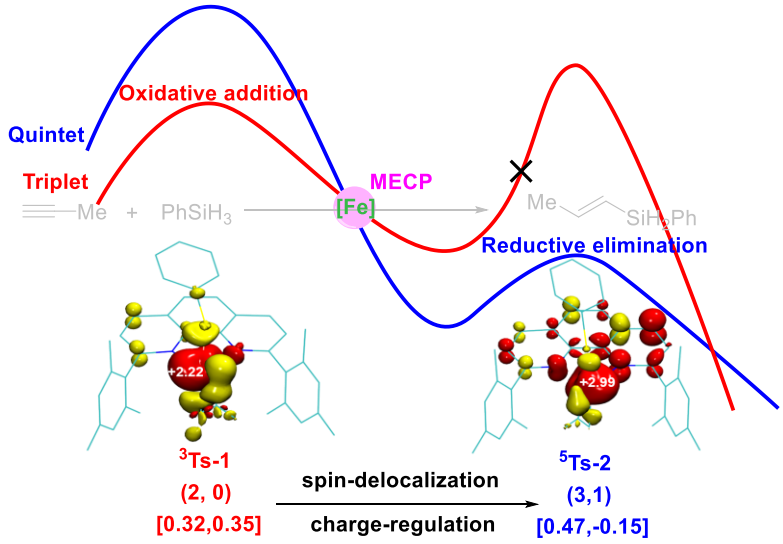

TOC

Teaser text: The electron spin-state effect in iron-catalysis was disclosed through a combination of experiments and theoretical calculations.

Introduction: Spin is an intrinsic property of electrons, and studies on electron spin have been at the forefront of materials science and interdisciplinary fields[1-4]. Spin crossover phenomena are common in open-shell metal complexes and have a wide range of applications in the field of materials science, such as spin-crossover sensors[5] and molecular spintronic materials[6]. In the field of transition metal catalysis, the effect of the catalyst spin state on chemical reactions has also received increasing attention[7-9]. Studies on the effect of the catalyst spin state are of great value for the development of first row transition metal (3d metal) catalysts. For a long time, precious metal catalysts, especially those based on 4d and 5d metals, have dominated the scientific research and production applications of transition metal catalysis. However, the scarce and non-renewable resources, high prices, and poor biocompatibility of 4d and 5d metals are increasingly becoming factors limiting their applications. Therefore, 3d metal catalysts, especially iron catalysts, have attracted much attention in recent years because of the abundant resources, low prices, and good biocompatibility of their central metals[10, 11]. The 3d metal catalysts and 4d or 5d metal catalysts have significant differences in electronic structures. According to crystal field theory, 4d or 5d metals, such as Pd and Pt, have large crystal field splitting energies and 4d or 5d metal complexes tend to be dominated by double electron transfer in the reaction with closed-shell electronic states. In such a case, the catalysts always maintain a single spin state (generally singlet), and the corresponding catalytic processes can be called “spin-constant catalysis”. By contrast, 3d metals, typically the iron, have small crystal field splitting energies, so 3d metal complexes are prone to form open-shell structures, which

usually have unique properties different from those of closed-shell metal catalysts[12]. Open-shell catalysts with different spin states might also have different catalytic properties[13]. Moreover, open-shell catalysts can undergo spin crossover in catalytic reactions, thus affecting the reaction process and showing a unique “two-state/multi-state reactivity” (TSR/MSR)[14]. Such catalytic processes can be called as “spin-crossover catalysis.” In fact, the promotion of reactions by spin crossover in 3d metal catalysis has been proposed for a long time and has been widely applied for explaining bioinorganic catalysis[15]. In recent years, the effect of spin state on transition metal catalysis has also received increasing attention[16-20]. Several unique properties of open-shell metal catalysts have been disclosed. For example, high-spin iron carbene, imido and oxo tend to have significant free radical properties and are prone to single electron transfer reactions[21-23]. The high spin catalyst's 3d-orbitals are occupied by unbonded electrons, making it immune to the common Lewis bases[18, 24]. The spin crossover effect of some open-shell catalysts has also been studied. For example, in the reactions of Fe/Co-catalyzed C-H bond activation, the transformation of catalyst from high spin state to low spin state provides a vacant metal 3d-orbital for the coordination and activation of C-H bond and the spin crossover in these processes may be partly attributed to the change of coordination shape of the catalysts[16-18, 20, 25-27]. Another research concluded that metal-oxo enzymes/synthetic reagents showed significant exchange-enhanced reactivity in the process of chemical bond activation[8]. There is no doubt that the above research has greatly promoted the understanding of the open-shell catalysts; however, little is known about how, exactly, the spin state affects

the reactivity and selectivity of catalysts, which has become a bottleneck in the development of 3d metal catalysis.

Recently, our research group has developed a series of iron complexes of 1,10-phenanthroline ligands, which can efficiently catalyze the addition reactions of various alkenes and alkynes[28-34], Not long ago, we reported the regioselectivity divergent hydrosilylation of alkynes catalyzed by the 1,10-phenanthroline-iron complex and found that the regioselectivity of the reaction could be completely reversed by simply changing the aryl substituent at the 2,9-position of the ligand (**Figure 1A**)[30]. In this study, we carried out in-depth research on the above reaction mechanism through the preparation and characterization of active catalysts combined with theoretical calculations. It was found for the first time that there is a typical two-state reactivity in the iron-catalyzed hydrosilylation of alkynes, in which a triplet iron catalyst promotes the oxidative addition process, while a quintet iron catalyst promotes the reductive elimination process. The prominent spin state effect of the iron catalyst is the fundamental reason for the excellent activity of the reaction. The active iron catalysts were synthesized and characterized by single-crystal X-ray diffraction, Mössbauer spectroscopy, X-ray photoelectron spectroscopy (XPS), and magnetic measurements, etc. to get deep insight into the electronic structure of Fe-phenanthroline complexes. It was found that the active iron catalysts exhibited almost the same catalytic performances with the corresponding catalyst precursors (reduced in situ) in the hydrosilylation of alkynes. We further established a “Central Metal Charge Analysis” (CMCA) method to study the deep-seated mechanism of oxidative addition and

reductive elimination promoted by the spin crossover of the iron catalyst. Combined experiments and calculations revealed that 1,10-phenanthroline, acting as a kind of redox active ligand, could promote the electron transfer between the iron center and the ligand through spin-delocalization and then adjust the oxidation state of the iron center to meet the electronic requirements of oxidative addition and reductive elimination. Finally, we also found that iron catalysts with specific spin states help achieving precise control of the regioselectivity by affecting multiple nonbonding interactions between ligands and substrates. Because spin delocalization not only facilitates the spin state crossover of the catalyst but also regulates the activity and selectivity of the catalyst, this spin state effect of the open-shell catalyst could be defined as "Spin Delocalization Regulated Reactivity" (SDRR). Although spin-delocalization has been reported in other iron catalysts with a redox-active ligand[35-37], little is known about how it affects catalytic properties. Since oxidative addition and reductive elimination are two important elementary steps in many transition metal catalysis, hopefully, the regulations of spin state effect disclosed in this study could be extended to other 2e redox catalysis promoted by other open-shell catalysts.

Results and Discussion

In a previous study[30], mixed-silane experiments showed that a hydrogen atom and a silyl group reacted with the C–C triple bond from the same silane (**Figure 1B**). This clearly indicated that the reaction was not initiated by Fe–H or Fe–Si species; otherwise, crossing-hydrosilylation products (**PA1-H**, **PB1-D, PA1'-H**, and **PB1'-D**) would be generated. Accordingly, an Fe(0)–Fe(II) catalytic cycle was then proposed (**Figure 1C**)

In this process, the catalyst precursor **CC** is reduced to Fe(0) by EtMgBr, which first coordinates with propyne and phenylsilane to form **Int-2**. **Int-2** then promotes the migration of hydrogen atoms on the phenylsilane to the C≡C triple bond via the transition state **Ts-1** by ligand-to-ligand hydrogen transfer to form **Int-3**. The **Int-3** then undergoes reductive elimination through **Ts-2** to afford **Int-4**. Finally, **Int-4** undergoes substrate exchange with the alkyne and silane to release the product **PC1** and re-generate **Int-2** for another catalytic cycle. It is always desirable to isolate an intermediate in the catalytic cycle, but such attempts usually fail because the intermediates are extremely active and short lived. Suboptimal goal to synthesis alkyne-coordinated iron complex also failed because both terminal and internal alkynes underwent trimerization to afford benzene derivatives. Finally, we prepared a series of alkene-coordinated formal Fe(0) complexes **CA1**, **CA2** and **CC1** (**Figure 1D**), analogues of **Int-4**. We measured the magnetic moments of the above catalysts both by Evans' method and with a superconducting quantum interference device (SQUID), and we found that the ground states of **CA1**, **CA2**, and **CC1** with diene coordination were triplet (S = 1). Meanwhile, DFT calculations revealed that the energies of triplet **CA1**, **CA2**, and **CC1** are lower than that of the corresponding quintet states, indicating triplet ground states. We next systematically evaluated the catalytic performances of these active Fe(0) catalysts in the hydrosilylation reaction of alkynes. All three Fe(0) complexes mentioned above were catalytically active without additional activator in the alkyne hydrosilylation reaction, giving almost the same result as the reaction promoted by the in-situ-generated catalyst from precursor **CA** and EtMgBr (**Figure 1E**).

No crossing-hydrosilylation products **PE1-H** or **PE2-D** were observed in the mixed-silane experiments (**Figure 1F**), consistent with the in-situ-activated system (**Figure 1B**). To further illustrate the kinetic performance of the active catalyst in the reaction, equal amounts of two different alkynes (**S4** and **S5**) were mixed with one equivalent of phenylsilane for the competitive hydrosilylation reaction. As a result, the hydrosilylation products (**PE1** and **PF1**) of the two alkynes had similar ratios when the reaction was catalyzed by the catalyst precursor **CA**/EtMgBr or by the pre-prepared active catalyst **CA1** (**Figure 1G**). These results indicate that the catalyst activated in situ exhibited comparable kinetics to those of the active iron complex, which fully indicates that Fe(0) was the active species (at least the main species) that initiated the reaction.

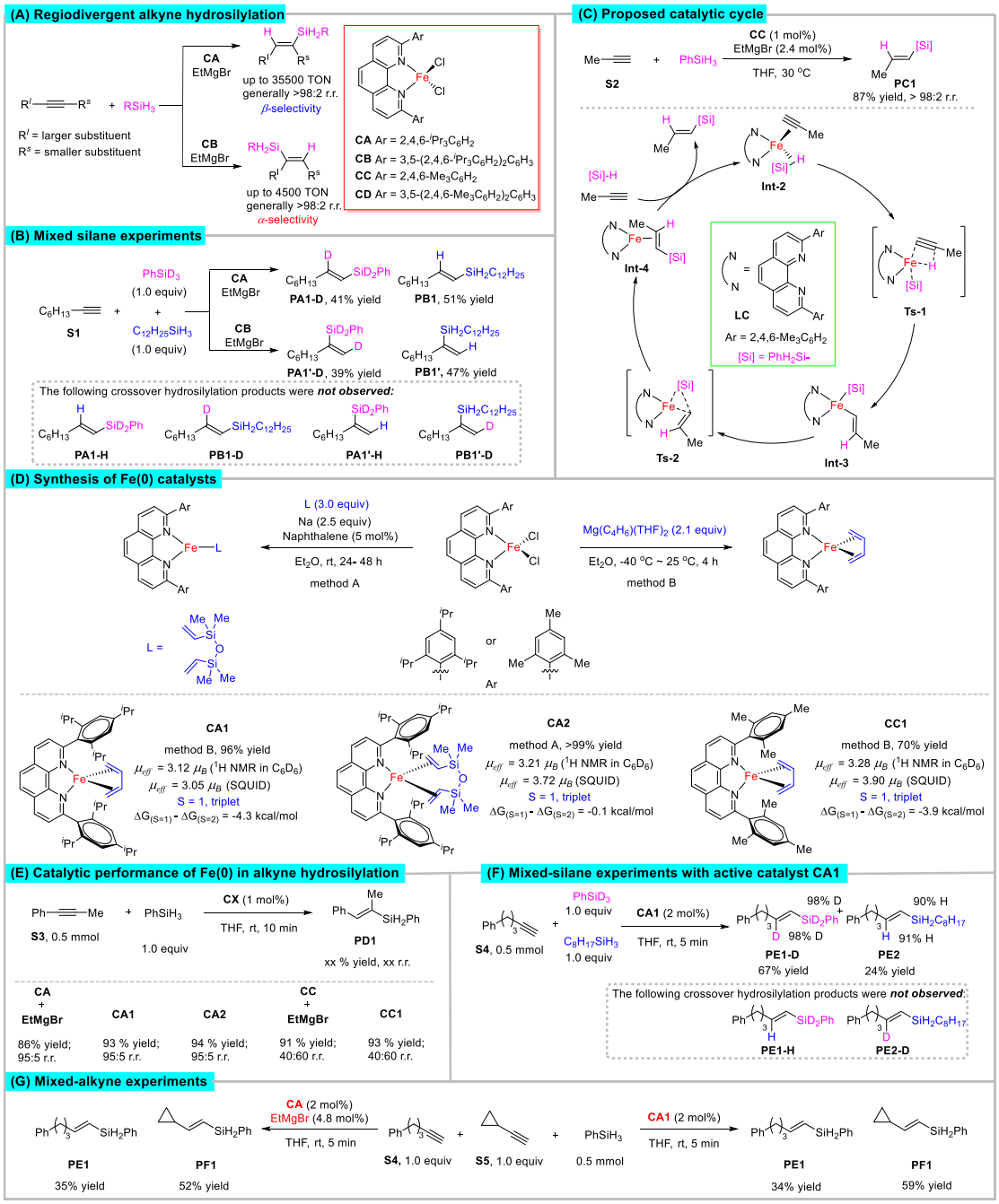

Figure 1. (A) Iron-catalyzed regiodivergent alkyne hydrosilylation from reference[30]. **(B)** Mixed silane experiments from reference[30]. **(C)** Proposed catalytic cycle. **(D)** Synthesis of Fe(0) catalysts; Magnetic moments were detected by Evans' method or superconducting quantum interference device (SQUID); DFT calculations were performed at ωB97XD/def2TZVPP-CPCM (THF) || ωB97XD/6-311g*-TZVP (Fe) level. **(E)** Catalytic performance of Fe(0) in alkyne hydrosilylation. **(F)** Mixed silane experiments with active catalyst **CA1**. **(G)** Mixed alkyne experiments.

We were fortunate to obtain single crystals of the Fe(0) complexes **CA1** (**Figure 2A**),

CA2 (**Figure 2B**) , and **CC1** (**Figure S24**), and we determined their chemical structures

by single-crystal X-ray diffraction. Comparing the crystal structures of the two Fe(0) complexes **CA1** and **CA2** with the Fe(II) precursor **CA** (**Figure 2C**), we found that the Fe-N bond lengths of the Fe(0) complexes were significantly shorter than those of the corresponding Fe(II) complexes. Relative to Fe(II) **CA** (2.1462(15) Å, on average), the average Fe-N bond lengths of **CA1** (1.985(6) Å, on average) and **CA2** (2.047(4) Å, on average) were shorter by 7.5% and 4.6%, respectively. The difference in bond lengths may be attributed to two factors. On the one hand, the spin multiplicity might affect the molecular electronic structure, thus leading to a difference in the bond lengths. Compared with the triplet complexes, the occupied ligand-directed (anti-bonding) d-orbitals in the quintet complex **CA** weakened and elongated the M-L bond[38]. On the other hand, the degrees of spin-delocalization in the complexes caused differences in the bond lengths. By examining the spin populations of these complexes, it was observed that large amounts of spin-delocalization occurred in both **CA1** and **CA2**. Namely, a large amount of spin delocalized from the iron center to the 1,10-phenanthroline backbone, while almost no spin-delocalization between the iron center and ligand occurred in **CA**. Spin-delocalization enhanced the metal–ligand interactions and thus shortened the Fe-N bond lengths of **CA1** and **CA2**[39, 40]. The C-N bond length of the 1,10-phenanthroline can also reflect the spin delocalization condition. The transfer of an electron from the metal to the ligand makes the ligand appear in a "reduced" state, so the C-N bond length of **CA1** and **CA2** increases significantly compared with **CA** (**Figure 2**)[41]. The above laws of Fe-N bond length, C-N bond length and spin delocalization are also applicable to **CC1** and **CC** (**Table S7**).

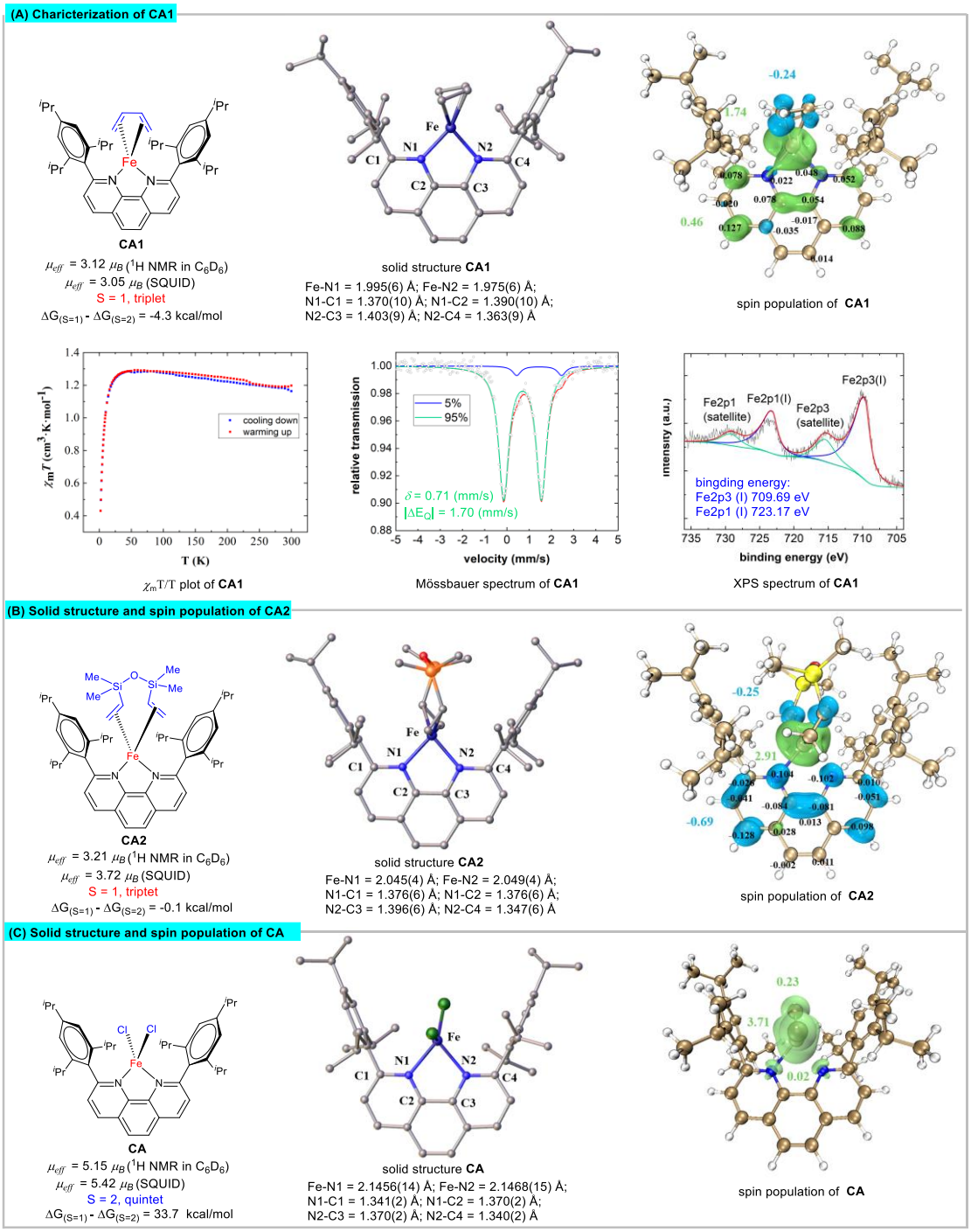

Figure 2. (A) Solid structure, spin populations (green, positive spin density; blue, negative spin density), magnetic property, Mössbauer and XPS spectra of **CA1**. **(B)** Solid structure and spin populations of **CA2**. **(C)** Solid structure and spin populations of **CA**.

In addition, although both **CA1** and **CA2** were triplet (S = 1) Fe(0) complexes, there was a significant difference in their Fe-N bond lengths, which we believe was due to the difference in their spin populations. The analysis of the spin populations of these

two complexes revealed that both had significant spin-delocalization from the iron center to the 1,10-phenanthroline ligand backbone. The difference was that the spin on 1,10-phenanthroline ligand in **CA1** (**Figure 2A**) was in the same direction as the spin on the iron center and the spin on the 1,10-phenanthroline in **CA2** (**Figure 2B**) was in the opposite direction as the spin on iron center, which led to a decrease and increase in the spin on the iron, respectively. For **CA1**, the net spin on the iron was 1.74, and for **CA2**, the net spin on the iron was 2.91. As mentioned above, the higher spin density on the iron center weakened the iron–ligand bonds, which is manifested by an increase in the Fe-N bond length. The above analyses clearly showed that the spin-delocalization function of 1,10-phenanthroline played a crucial role in the regulation of the spin state of the iron atom. Taking **CA1** as an example, further characterization was carried out to understand the electronic structure of Fe-phenanthroline complexes. The low-temperature drop of the $\chi_m T/T$ curve was likely a result of zero-field splitting (D), indicating strong magnetic coupling between the iron and radical anion on ligand. Large D may be responsible for the EPR silent fact of all the three active complexes (**Figure 2A**)[42]. Fitting to the Mössbauer spectrum give parameters δ = 0.71 and $|\Delta E_Q|$ = 1.70 mm/s with 5% impurity. Combined with spin population, this was identified as a $S_{(Fe)}$ = 1/2 Fe (I) complex, similar to a reported β-diketiminate-Fe complex[43]. Calculated Mössbauer parameters (δ = 0.60 and $|\Delta E_Q|$ = 1.97 mm/s, **Table S1**) using Holland's calibration[44] by ORCA[45] were in reasonable error with experimental data. Careful measurement of XPS spectrum afforded 709.69 eV Fe2p3 binding energy, slightly lower than that of $FeCl_2$ (710.40 eV). Combined with XRD structure, Mössbauer

spectrum, magnetic property measurement and DFT calculations, this was best described as a Fe(I) species. It is clear that spin-delocalization between the iron and the 1,10-phenanthroline is responsible for the elevated oxidation state of the formal Fe(0) species.

In summary, the above structural analyses indicated that the 1,10-phenanthroline ligand backbone had a good spin-delocalization function, which efficiently regulate both the spin state and oxidation state of the iron atom. This might be the electronic structural basis for the pronounced spin-state effect of the iron-catalyzed alkyne hydrosilylation reaction.

Spin state effect on catalytic activity

We performed DFT calculations for further understanding the catalytic behaviors of the open-shell iron catalyst in alkyne hydrosilylation **(Figure 3)**. Since the reactions affording α-selectivity and β-selectivity had similar mechanisms, we only discussed the β-selective reaction in the main text and included the calculation data of α-selective reaction in the SI.

DFT calculations showed that the singlet potential energy surface is always at the highest position throughout the reaction, so the reaction is more likely to proceed on the triplet and quintet potential energy surfaces. It is likely that the catalyst precursors coordinate mainly with two alkynes after being reduced to Fe(0). In the subsequent oxidative addition step (**Int-2**–**Ts-1**–**Int-3**), the $\Delta G^{\neq}$ values of the triplet and quintet transition state **Ts-1** relative to ^{3}**Int-1** are 15.9 and 26.9 kcal/mol, respectively. In the

oxidative addition process, both the intermediates and transition states in the triplet are more energetically favorable than those in the quintet. In the reductive elimination process, the situation is totally reversed, as **^{5}Int-3** and **^{5}Ts-2** are much lower in energy than **^{3}Int-3'** and **^{3}Ts-2**, respectively. As a result, the reductive elimination process takes place on the quintet potential energy surface to afford **^{5}Int-4**. Based on the above analysis, this reaction has a typical two-state reactivity. Overall, the spin crossover results in a decrease of the reaction energy barrier by 8.4 kcal/mol (from 24.3 to 15.9 kcal/mol), which greatly accelerates the reaction rate. We located a minimum energy crossing point (MECP)[46-48] between the triplet and quintet, which lies between **^{3}Int-3'** (or **^{3}Ts-1**) and **^{5}Int-3** along the reaction pathway. Since the MECP is not a stationary point on the potential energy surface, the normal frequency analysis is not physically meaningful. Thus, we calculated the projected frequency[49] in the direction of the reaction pathway to estimate the Gibbs free energy correction and then estimated the relative Gibbs free energy of the MECP (11.5 kcal/ mol). Since MECP is highly similar to **^{3}Int-3'** in structure, **^{3}Int-3'** is most likely to have been formed through **^{3}Ts-1**, which then undergoes a spin crossover to afford **^{5}Int-3** via MECP. An alternative possible pathway is that **^{5}Int-3** is formed through MECP directly from **^{3}Ts-1** without forming **^{3}Int-3'**. Since the difference in energy between MECP and **^{3}Int-3'** is small (1.1 kcal/ mol), this may indicate a fast spin-crossover rate here, which is consistent with the fast experimental reaction rate (TOF 35.5 s^{-1})[30].

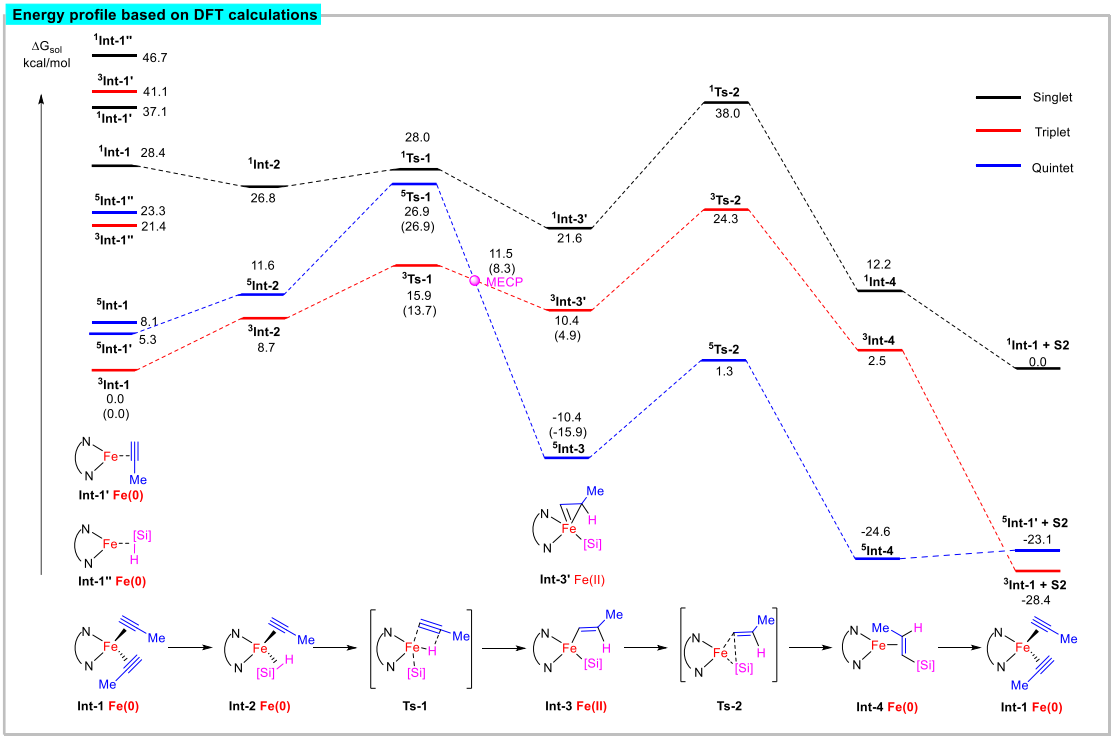

Figure 3. Energy profiles based on DFT calculations. Numbers in parenthesis denote electronic energies of the structure. DFT calculation were performed at ωB97XD/def2TZVPP-CPCM (THF) || ωB97XD/6-31G*-TZVP (Fe) level. Energies were reported in kcal/mol.

To further understand the mechanism that a triplet iron catalyst promotes the oxidative addition process while a quintet iron catalyst promotes the reductive elimination process, a simple but effective index, charge-of-central-metal, was set up to measure both elementary steps based on DFT calculation. In a transition metal-catalyzed reactions, the mechanism of the oxidative addition step is usually the filling of the d electrons of the metal into the anti-bond orbitals of the σ or π coordination bonds, thus weakening their bond strength and breaking their σ or π bonds to achieve the oxidative addition to the metal atoms. Therefore, the higher the electron density on the central metal is, the more likely oxidative addition is to occur. The reductive elimination is the reverse process of oxidative addition. The lower the electron density on the central metal is, the more likely the reductive elimination is to occur. Based on this, we

established the “Central Metal Charge Analysis” (CMCA) method to understand the spin state effect on the oxidative addition and reductive elimination processes. The basic principle for the CMCA method is that a lower charge on central metal (lower oxidation state) favors oxidative addition, and a higher charge on central metal (higher oxidation state) favors reductive elimination.

We first performed charge population analysis of some key intermediates and transition states related to oxidative addition and reductive elimination (**Figure 4A**). According to CMAC, the iron center of oxidative addition transition state **Ts-1** had a lower charge in the triplet state (^{3}**Ts-1**, 0.32) than in the corresponding quintet state (^{5}**Ts-1**, 0.50), and thus, the triplet ^{3}**Ts-1** with a higher electron density on the iron center favored the oxidative addition process. The variation of the charge on the 1,10-phenanthroline ligand backbone from **Int2** to **Ts1** (ligand charge variation in triplet potential energy surface, **Int2**–**Ts1**: −0.27 to 0.35; quintet potential energy surface, **Int2**–**Ts1**: −0.34 to −0.20) revealed the origin of the above metal charge difference. The iron center of the triplet iron catalyst apparently took a larger number of electrons from the ligand than its quintet counterpart. Thus, the triplet iron catalyst was more favorable for the oxidative addition. The above phenomenon was further confirmed by the spin population analysis from **Int2** to **Ts1** (**Figure 4A**). The spin population changed from ^{3}**Int-2** (3, -1) to ^{3}**Ts-1** (2, 0), indicating a ligand β-electron transfer to the metal center, resulting in the charge on Fe changing from 0.63 to 0.32, promoting oxidative addition. In contrast, there was no significant change in the catalyst charge and spin population from ^{5}**Int-2** to ^{5}**Ts-1** (**Table S12**) under the quintet potential energy surface. In the

reductive elimination process, an α-electron on Fe was transferred to the ligand during the process of ^{5}**Int-3** (4, 0) to ^{5}**Ts-2** (3, 1). However, in the triplet potential energy surface, there was no significant change in the electron spin and charge population from ^{3}**Int-3'** to ^{3}**Ts-2**. As a result, the metal charge of the quintet transition state ^{5}**Ts-2** was 0.47, which was higher than the metal charge of the triplet transition state ^{3}**Ts-2** (0.15), thus making it easier for reductive elimination to occur.

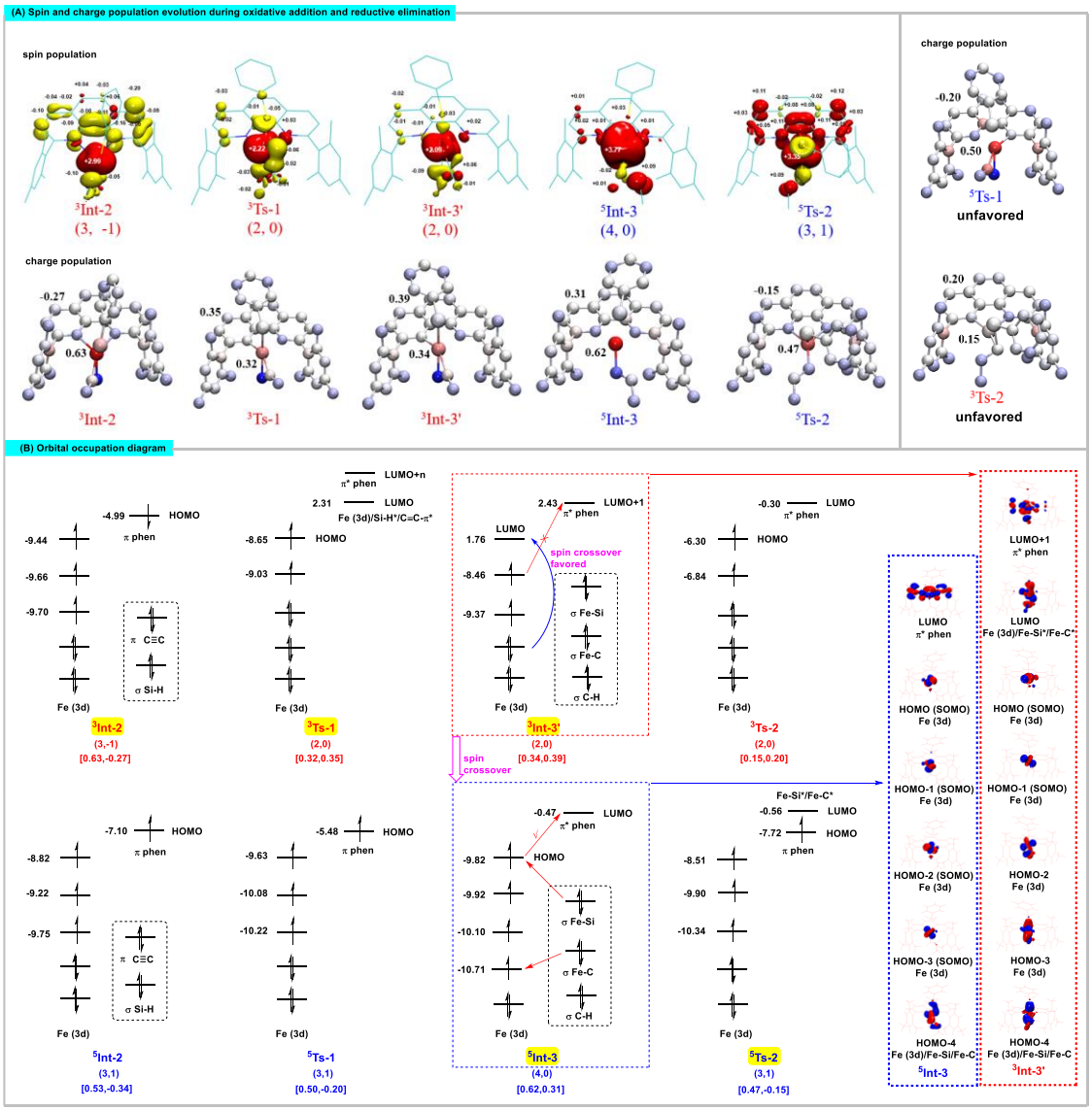

Figure 4. (A) Mulliken spin (red, spin up; yellow, spin down) and charge (red, positive charge; blue, negative charge; darker colour indicates larger charge) population evolution during reaction. The (m, n) labelling denotes the number of the unpaired

electrons on the iron (m) and the ligand backbone (n), and the negative sign for n indicates antiferromagnetic coupling between the iron and the ligand. **(B)** Calculated molecular orbital occupation diagram and part of the frontier orbitals treated by wavefunction biorthogonalization. Orbital energies (eV) were evaluated for qualitative discussion. The [m, n] labelling denotes the charge on the iron (m) and the ligand backbone (n).

To further investigate the electron transfer process between the ligand and iron center and reveal the influence of the catalyst spin states on the reaction, we made a molecular orbital occupation diagram by wavefunction biorthogonalization[50] (**Figure 4. B**). As above mentioned, the electron transfer from the ligand to the metal during the oxidative addition process lowered the metal oxidation state to facilitate this process. By analyzing the orbital occupation diagram, unpaired electrons were found on both ligand backbones of ^{3}**Int-2** and ^{5}**Int-2**. The difference was that the unpaired electron on the ligand of ^{3}**Int-2** had the opposite spin direction as the unpaired electrons on the metal, while the unpaired electrons on the ligand of ^{5}**Int-2** had the same spin direction as the unpaired electrons on the metal. According to the Pauli exclusion principle, there was no suitable iron singly occupied orbital or empty orbital in ^{5}**Int-2** that could accommodate α-electrons on the 1,10-phenanthroline, and the electron transfer from the ligand to the metal was more favorable in ^{3}**Int-2** than in ^{5}**Int-2**. Thus, the oxidative addition step proceeded at the triplet potential energy surface. The LUMO of ^{3}**Ts-1** showed strong iron 3d-orbital interacting with Si-H* antibonding orbital and C≡C* antibonding orbital (activating Si-H and C≡C), promoting the transfer of hydrogen atom to alkyne, giving ^{3}**Int-3'**. Similarly, the electron transfer from the metal to the ligand during the reductive elimination elevated the metal oxidation state to facilitate this process. Although the phenanthroline ligand in both ^{3}**Int-3'** and ^{5}**Int-3** had the potential

to accept an electron from iron center and thus to elevate the oxidation state of iron center, the low-lying Fe 3d-orbital (LUMO, 1.76 eV) in **^{3}Int-3'** made the electron transfer difficult (the energy gap between HOMO and π* phen orbital was 10.89 eV). As a result, there was no obvious spin-delocalization in **^{3}Ts-2**, and all 3d-orbitals of iron were occupied, so the oxidation state of Fe is very low (0.15), (energy barrier for reductive elimination was 13.9 kcal/mol, **Figure 3**). On the other hand, this low-lying Fe 3d-orbital provided condition for the spin crossover from triplet to quintet. In contrast to **^{3}Int-3'**, 3d-orbitals of iron in **^{5}Int-3** were all occupied, and the band gap between π* phen orbital (-0.47) and HOMO (-9.82) is 9.35 eV, which was lower than that of **^{3}Int-3'** (10.89 eV). Therefore, there was significant spin-delocalization in the subsequent **^{5}Ts-2**, which made the the net charge of iron in **^{5}Ts-2** decreased from 0.62 to 0.47. Moreover, the LUMO of **^{5}Ts-2** was mainly composed of Fe-Si* and Fe-C* antibonding orbitals, which was favorable for reduction elimination (11.7kcal/mol, **Figure 3**).

Overall, in this Fe-catalyzed alkyne hydrosilylation reaction, the 1,10-phenanthroline with a large planar conjugated structure serves as a typical redox non-innocent ligand. It acts as an electron reservoir to regulate the spin states and oxidation states of the central metal, thus adapting to the electrostatic demands of both the oxidative addition and reductive elimination processes. The ligand acts as an electron donor to lower the oxidation state of the iron atom, facilitating the oxidative addition process that occurs on the triplet potential energy surface, while acting as an electron acceptor to elevate the oxidation state of the iron atom, facilitating the reductive elimination process that

occurs on the quintet potential energy surface. Most importantly, a spin crossover from the triplet state to the quintet state is necessary to help realize such an electron transfer process. It is important to point out that traditional methods such as ligand modification with some electron with-drawing/donating group can hardly accelerate the oxidative addition and reductive elimination processes simultaneously because these two processes have opposite electrostatic demand. The SDRR enabled simultaneous acceleration of the processes with opposite electrostatic demand in iron catalysis might also be a key to understand the other spin-crossover catalysis.

Effect of spin state on regioselectivity

To further understand the origin of the regioselectivity, independent gradient model analysis based on a Hirshfeld partition (IGMH) [51] (**Figure 5. A**) and interaction region indicator **(**IRI) [52] analysis (**Figure 5. B**) were performed using VMD [53] and Multiwfn [50] to analyze the noncovalent intramolecular interactions of **Ts1**, the key transition state that determines regioselectivity.

The methyl group on the ligand formed a crowded interspace on the lateral position of the iron. When the alkyne was heading downward (^{3}**Ts-1a,** leading to α-selectivity), the methyl group of the alkyne fell into this crowded interspace, forming a large repulsive interaction. This repulsive interaction was greatly released when the alkyne was heading upward (^{3}**Ts-1,** leading to β-selectivity). As a result, β-selectivity was 3.5 kcal/mol favored than α-selectivity (**Figure 5. A**).

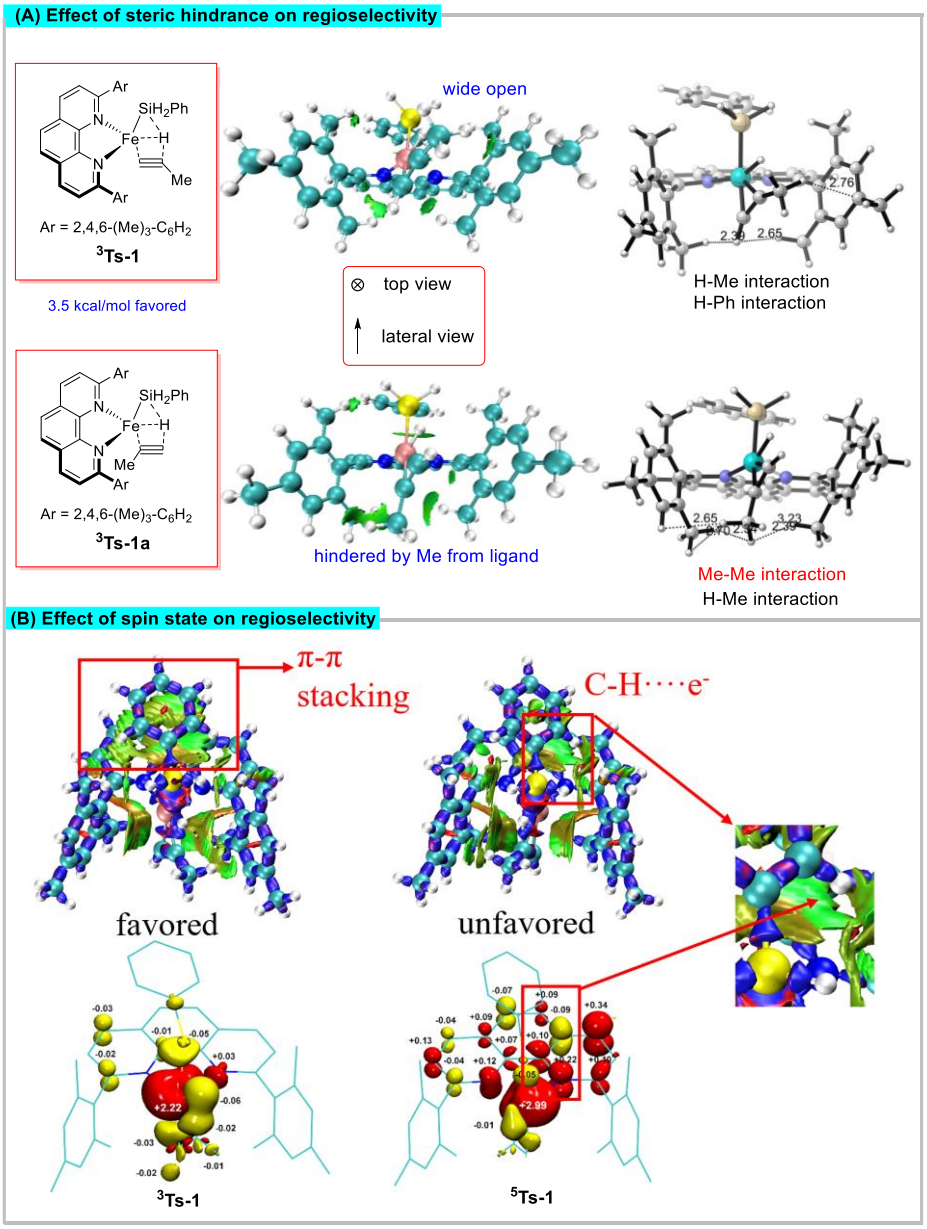

Figure 5. (A) Noncovalent interaction analysis of key transition states that determine regioselectivity by IGMH. The green sheets represent intramolecular noncovalent interactions. Larger sheets indicate greater noncovalent interactions. Some representative distances between atoms and fragments are shown in units of Å. **(B)** Intramolecular interaction analysis by IRI and spin population of **^{3}Ts-1** and **^{5}Ts-1**.

To understand how spin states affect regioselectivity, IRI analysis (**Figure 5. B**) was applied to investigate the intramolecular interaction of both **^{3}Ts-1** and **^{5}Ts-1**. It seemed clear that there was no significant difference between **^{3}Ts-1** and **^{5}Ts-1,** except for the distinct π–π stacking interaction on **^{3}Ts-1 (**π–π stacking the 1,10-phenanthroline

backbone and the phenyl group of hydrosilane**),** which was likely to play an important role in stabilizing the transition state. This π–π stacking interaction was inhibited in **^{5}Ts-1**， likely replaced by the weak electrostatic interaction between C-H bond and unbonded electron on ligand. This can be seen directly from the structure of **^{3}Ts-1** and **^{5}Ts-1.** The 1,10-phenanthroline backbone in **^{5}Ts-1** was clearly not parallel to the phenyl group of the hydrosilane. The real question was the reason for this structure difference. Once again, we think this could be attributed to spin-delocalization. By comparing the spin populations (**Figure 5. B**) of **^{3}Ts-1** and **^{5}Ts-1**, we found that a large amount of spin on the iron in **^{5}Ts-1** delocalized to the 1,10-phenanthroline backbone, leaving a large amount of negative charge on the 1,10-phenanthroline backbone. Consequently, the π–π stacking that stabilized the transition states was suppressed by electrostatic repulsion. However, in **^{3}Ts-1,** there was rarely no spin-delocalization from the iron to the ligand, and the π–π stacking was not affected.

The above analysis concludes that, in addition to the effect of steric hindrance, the catalyst's spin state also has an impact on the realization of regioselectivity of the reaction. A catalyst with a specific spin state can adjust the intramolecular noncovalent interactions of the transition state by controlling the spin-delocalization, enhancing the stability of the transition state, and then influencing the reaction process to achieve precise control of the regioselectivity.

Conclusion

In conclusion, we have systematically investigated the mechanism of the iron-catalyzed hydrosilylation of alkynes and found that iron catalysts could promote oxidative

addition and reductive elimination processes and enhance the transition state stability through spin-delocalization. We synthesized and characterized the electronic structure of the well-defined formal Fe(0)-phenanthroline complexes to reveal the unique electronic structure of the catalysts. We developed the "Central Metal Charge Analysis" method as an effective index to help understand the spin state effect in elementary steps of the reaction, which revealed that the redox non-innocent 1,10-phenanthroline acted as an electron donor and acceptor that regulated the oxidation state of the iron center by spin-delocalization to meet the opposite electrostatic requirements of oxidative addition and reductive elimination, respectively, thus facilitating the reaction. The spin crossover of the iron catalyst was the key to facilitating the above electron transfer. The precise regulation of the regioselectivity relied on the unique active cavity formed near the iron center by the ligand's steric effect and was enhanced by stabilization of the transition state by specific spin state. These unique spin state effects were designed as "Spin-delocalization Regulated Reactivity" (SDRR). The above findings have important implications for understanding the mechanisms of iron-catalyzed reactions, the spin-state effect of open-shell catalysts, and the development of new iron catalysts and other Earth-abundant metal catalysts.

Data availability: All data are available in the main text or the supplementary materials.

Acknowledgments: We thank Prof. Wei Shi (NKU, magnetic moment measurement), Dr. Yin Yang (NKU, electron paramagnetic resonance measurement), Prof. Xiao-Song Xue (NKU, helpful discussion on DFT calculation), Prof. Qian Peng (NKU, helpful discussion on DFT calculation), Prof. Hui Chen (ICC, DFT calculation examination), Xiao-Shuang Gou (NKU, magnetic moment measurement and X-ray single crystal structural analyses), Zhong-Hang Chen (NKU, X-ray single crystal structural analyses), and Hao-Yang Jiang (NKU, X-ray photoelectron spectroscopy) for their generous help.

Funding: This work was supported by the National Key R&D Program of China (2021YFA1500200), National Natural Science Foundation of China (22001129, 92156006, 21971119), "111" project (B06005) of the Ministry of Education of China, Haihe Laboratory of Sustainable Chemical Transformations, and Fundamental Research Funds.

Author contributions: Conceptualization: SFZ, PH, MYH. Methodology: SFZ, PH, MYH, JHL, TZQ, YLL. Investigation: SFZ, PH, MYH, JHL, TZQ, YLL. Visualization: PH, MYH. Funding acquisition: SFZ, MYH. Project administration: SFZ. Supervision: SFZ. Writing – original draft: SFZ, PH, MYH. Writing – review & editing: SFZ, PH, MYH, JHL, TZQ, YLL.

Competing interests: Conflict of interest statement. None declared.

References

1. Naaman R, Paltiel Y, Waldeck DH. Chiral molecules and the electron spin. *Nat Rev Chem*. 2019; **3**(4): 250-60. doi: 10.1038/s41570-019-0087-1

2. Coronado E. Molecular magnetism: from chemical design to spin control in molecules, materials and devices. *Nat Rev Mater*. 2019; **5**(2): 87-104. doi: 10.1038/s41578-019-0146-8

3. Gaita-Arino A, Luis F, Hill S *et al.* Molecular spins for quantum computation. *Nat Chem*. 2019; **11**(4): 301-9. doi: 10.1038/s41557-019-0232-y

4. Banerjee-Ghosh K, Ben Dor O, Tassinari F *et al.* Separation of enantiomers by their enantiospecific interaction with achiral magnetic substrates. *Science*. 2018; **360**(6395): 1331-4. doi: 10.1126/science.aar4265

5. Brooker S. Spin crossover with thermal hysteresis: practicalities and lessons learnt. *Chem Soc Rev*. 2015; **44**(10): 2880-92. doi: 10.1039/c4cs00376d

6. Kim YH, Zhai Y, Lu H *et al.* Chiral-induced spin selectivity enables a room-temperature spin light-emitting diode. *Science*. 2021; **371**(6534): 1129-33. doi: 10.1126/science.abf5291

7. Poli R. Open-shell organometallics as a bridge between Werner-type and low-valent organometallic complexes. the effect of the spin state on the stability, reactivity, and structure. *Chem Rev*. 1996; **96**(6): 2135-204. doi: 10.1021/cr9500343

8. Shaik S, Chen H, Janardanan D. Exchange-enhanced reactivity in bond activation by metal-oxo enzymes and synthetic reagents. *Nat Chem*. 2011; **3**(1): 19-27. doi: 10.1038/nchem.943

9. Fürstner A. Iron catalysis in organic synthesis: a critical assessment of what it takes to make this base metal a multitasking champion. *ACS Cent Sci*. 2016; **2**(11): 778-89. doi: 10.1021/acscentsci.6b00272

10. Bauer I, Knolker HJ. Iron catalysis in organic synthesis. *Chem Rev*. 2015; **115**(9): 3170-87. doi: 10.1021/cr500425u

11. Rana S, Biswas JP, Paul S *et al.* Organic synthesis with the most abundant transition metal-iron: from rust to multitasking catalysts. *Chem Soc Rev*. 2021; **50**(1): 243-472. doi: 10.1039/d0cs00688b

12. Glascoe EA, Sawyer KR, Shanoski JE *et al.* The influence of the metal spin state in the iron-catalyzed alkene isomerization reaction studied with ultrafast infrared spectroscopy. *J Phys Chem C*. 2007; **111**(25): 8789-95. doi: 10.1021/jp068576j

13. Shaver MP, Allan LE, Rzepa HS *et al.* Correlation of metal spin state with catalytic reactivity: polymerizations mediated by alpha-diimine-iron complexes. *Angew Chem Int Ed*. 2006; **45**(8): 1241-4. doi: 10.1002/anie.200502985

14. Schroder D, Shaik S, Schwarz H. Two-state reactivity as a new concept in organometallic chemistry. *Acc Chem Res*. 2000; **33**(3): 139-45. doi: 10.1021/ar990028j

15. Shaik S, Hirao H, Kumar D. Reactivity of high-valent iron-oxo species in enzymes and synthetic reagents: a tale of many states. *Acc Chem Res*. 2007; **40**(7): 532-42. doi: 10.1021/ar600042c

16. Holland PL. Distinctive reaction pathways at base metals in high-spin organometallic catalysts. *Acc Chem Res*. 2015; **48**(6): 1696-702. doi: 10.1021/acs.accounts.5b00036

17. Kim D, Pillon G, DiPrimio DJ *et al.* Highly Z-selective double bond transposition in simple alkenes and allylarenes through a spin-accelerated allyl mechanism. *J Am Chem Soc*. 2021; **143**(8): 3070-4. doi: 10.1021/jacs.1c00856

18. Lutz SA, Hickey AK, Gao Y *et al.* Two-state reactivity in iron-catalyzed alkene isomerization confers sigma-base resistance. *J Am Chem Soc*. 2020; **142**(36): 15527-35. doi: 10.1021/jacs.0c07300

19. Hu L, Chen H. Substrate-dependent two-state reactivity in iron-catalyzed alkene [2+2] cycloaddition reactions. *J Am Chem Soc*. 2017; **139**(44): 15564-7. doi: 10.1021/jacs.7b06086

20. Sun Y, Tang H, Chen K *et al.* Two-state reactivity in low-valent iron-mediated c-h activation and the implications for other first-row transition metals. *J Am Chem Soc*. 2016; **138**(11): 3715-30. doi: 10.1021/jacs.5b12150

21. King ER, Hennessy ET, Betley TA. Catalytic C-H bond amination from high-spin iron imido complexes. *J Am Chem Soc*. 2011; **133**(13): 4917-23. doi: 10.1021/ja110066j

22. Liu J, Hu L, Wang L *et al.* An Iron(II) Ylide complex as a masked open-shell iron alkylidene species in its alkylidene-transfer reactions with alkenes. *J Am Chem Soc*. 2017; **139**(10): 3876-88. doi: 10.1021/jacs.7b00484

23. Saouma CT, Peters JC. M≡E and M=E complexes of iron and cobalt that emphasize three-fold symmetry (E≡O, N, NR). *Coord Chem Rev*. 2011; **255**(7-8): 920-37. doi: 10.1016/j.ccr.2011.01.009

24. Gao Y, Carta V, Pink M *et al.* Catalytic carbodiimide guanylation by a nucleophilic, high spin iron(ii) imido complex. *J Am Chem Soc*. 2021; **143**(14): 5324-9. doi: 10.1021/jacs.1c02068

25. Bellows SM, Cundari TR, Holland PL. Spin crossover during β-hydride elimination in high-spin iron(II)– and cobalt(II)–alkyl complexes. *Organometallics*. 2013; **32**(17): 4741-51. doi: 10.1021/om400325x

26. Macaulay CM, Gustafson SJ, Fuller JT *et al.* Alkene isomerization–hydroboration catalyzed by first-row transition-metal (Mn, Fe, Co, and Ni) N-phosphinoamidinate complexes: origin of reactivity and selectivity. *ACS Catal*. 2018; **8**(11): 9907-25. doi: 10.1021/acscatal.8b01972

27. Garhwal S, Kaushansky A, Fridman N *et al.* Part per million levels of an anionic iron hydride complex catalyzes selective alkene isomerization via two-state reactivity. *Chem Catal*. 2021; **1**(3): 631-47. doi: 10.1016/j.checat.2021.05.002

28. Hu M-Y, He Q, Fan S-J *et al.* Ligands with 1,10-phenanthroline scaffold for highly regioselective iron-catalyzed alkene hydrosilylation. *Nat Commun*. 2018; **9**(1): 221-31. doi: 10.1038/s41467-017-02472-6

29. Hu M-Y, Lian J, Sun W *et al.* Iron-catalyzed dihydrosilylation of alkynes: efficient access to geminal bis(silanes). *J Am Chem Soc*. 2019; **141**(11): 4579-83. doi: 10.1021/jacs.9b02127

30. Hu M-Y, He P, Qiao T-Z *et al.* Iron-catalyzed regiodivergent alkyne hydrosilylation. *J Am Chem Soc*. 2020; **142**(39): 16894-902. doi: 10.1021/jacs.0c09083

31. Huang Q, Su Y-X, Sun W *et al.* Iron-catalyzed vinylzincation of terminal alkynes. *J Am Chem Soc*. 2022; **144**(1): 515-26. doi: 10.1021/jacs.1c11072

32. Sun W, Li M-P, Li L-J *et al.* Phenanthroline-imine ligands for iron-catalyzed alkene hydrosilylation. *Chem Sci*. 2022; **13**(9): 2721-8. doi: 10.1039/d1sc06727c

33. Li W-T, Hu M-Y, Xiong J-W *et al.* Iron-catalysed hydroalumination of internal alkynes. *Chem Sci*. 2022; **13**(26): 7873-9. doi: 10.1039/d2sc02160a

34. Huang Q, Su Y-X, Sun W *et al.* Iron-catalyzed alkylzincation of terminal alkynes. *ACS Catal*. 2022; **12**(4): 2581-8. doi: 10.1021/acscatal.1c05870

35. Chirik PJ, Wieghardt K. Chemistry. Radical ligands confer nobility on base-metal catalysts. *Science*. 2010; **327**(5967): 794-95. doi: 10.1126/science.1183281

36. Lyaskovskyy V, de Bruin B. Redox non-innocent ligands: versatile new tools to control catalytic reactions. *ACS Catal*. 2012; **2**(2): 270-9. doi: 10.1021/cs200660v

37. Hohenberger J, Ray K, Meyer K. The biology and chemistry of high-valent iron-oxo and iron-nitrido complexes. *Nat Commun*. 2012; **3**: 720-33. doi: 10.1038/ncomms1718

38. Kepp KP. Consistent descriptions of metal–ligand bonds and spin-crossover in inorganic chemistry. *Coord Chem Rev*. 2013; **257**(1): 196-209. doi: 10.1016/j.ccr.2012.04.020

39. Seo J, Braun JD, Dev VM *et al.* Driving barocaloric effects in a molecular spin-crossover complex at low pressures. *J Am Chem Soc*. 2022; **144**(14): 6493-503. doi: 10.1021/jacs.2c01315

40. Guionneau P. Crystallography and spin-crossover. A view of breathing materials. *Dalton Trans*. 2014; **43**(2): 382-93. doi: 10.1039/c3dt52520a

41. Bart SC, Chlopek K, Bill E *et al.* Electronic structure of bis(imino)pyridine iron dichloride, monochloride, and neutral ligand complexes: a combined structural, spectroscopic, and computational study. *J Am Chem Soc*. 2006; **128**(42): 13901-12. doi: 10.1021/ja064557b

42. Yang P-C, Yu K-P, Hsieh C-T *et al.* Stabilization of a high-spin three-coordinate Fe(III) imidyl complex by radical delocalization. *Chem Sci*. 2022; **13**(33): 9637-43. doi: 10.1039/d2sc02699f

43. Dugan TR, Bill E, MacLeod KC *et al.* Synthesis, spectroscopy, and hydrogen/deuterium exchange in high-spin iron(II) hydride complexes. *Inorg Chem*. 2014; **53**(5): 2370-80. doi: 10.1021/ic4013137

44. McWilliams SF, Brennan-Wydra E, MacLeod KC *et al.* Density functional calculations for prediction of Fe-57 Mossbauer isomer shifts and quadrupole splittings in beta-diketiminate complexes. *ACS Omega*. 2017; **2**(6): 2594-606. doi: 10.1021/acsomega.7b00595

45. Neese F. Software update: the ORCA program system, version 4.0. *WIREs Comput Mol Sci*. 2017; **8**(1): e1327. doi: 10.1002/wcms.1327

46. Lu T. sobMECP program. http://sobereva.com/286 (2018).

47. Harvey JN, Aschi M, Schwarz H *et al.* The singlet and triplet states of phenyl cation. A hybrid approach for locating minimum energy crossing points between non-interacting potential energy surfaces. *Theor Chem Acc*. 1998; **99**: 95-9. doi: 10.1007/s002140050309

48. Harvey JN, Aschi M. Spin-forbidden dehydrogenation of methoxy cation: a statistical view. *Phys Chem Chem Phys*. 1999; **1**(24): 5555-63. doi: 10.1039/a907723e

49. Liu Z, Cheng R, He X *et al.* DFT functional benchmarking on the energy splitting of chromium spin states and mechanistic study of acetylene cyclotrimerization over the Phillips Cr(II)/silica catalyst. *J Phys Chem A*. 2012; **116**(28): 7538-49. doi: 10.1021/jp302529q

50. Lu T, Chen F. Multiwfn: a multifunctional wavefunction analyzer. *J Comput Chem*. 2012; **33**(5): 580-92. doi: 10.1002/jcc.22885

51. Lu T, Chen Q. Independent gradient model based on Hirshfeld partition: A new method for visual study of interactions in chemical systems. *J Comput Chem*. 2022; **43**(8): 539-55. doi: 10.1002/jcc.26812

52. Lu T, Chen Q. Interaction Region Indicator: A simple real space function clearly revealing both chemical bonds and weak interactions**. *Chem–Methods*. 2021; **1**(5): 231-9. doi: 10.1002/cmtd.202100007

53. Humphrey W, Dalke A, Schulten K. VMD: Visual molecular dynamics. *J Mol Graph*. 1996; **14**(1): 33-8. doi: 10.1016/0263-7855(96)00018-5